Composite Structures 92 (2010) 1813–1822

Contents lists available at ScienceDirect

Composite Structures

journal homepage: www.elsevier.com/locate/compstruct

Autofrettage of layered and functionally graded metal–ceramic composite vessels

B. Haghpanah Jahromi, A. Ajdari, H. Nayeb-Hashemi, A. Vaziri *

Department of Mechanical and Industrial Engineering, Northeastern University, Boston, MA 02115, USA

ARTICLE INFO

Article history:
Available online 2 February 2010

Keywords:
Autofrettage
Pressure vessel
Layered composites
Functionally graded material
Variable Material Properties method

ABSTRACT

The residual compressive stresses induced by the autofrettage process in a metal vessel are limited by metal plasticity. Here we showed that the autofrettage of layered metal–ceramic composite vessels leads to considerably higher residual compressive stresses compared to the counterpart metal vessel. To calculate the residual stresses in a composite vessel, an extension of the Variable Material Properties (X-VMP) method for materials with varying elastic and plastic properties was employed. We also investigated the autofrettage of composite vessels made of functionally graded material (FGM). The significant advantage of this configuration is in avoiding the negative effects of abrupt changes in material properties in a layered vessel – and thus, inherently, in the stress and strain distributions induced by the autofrettage process. A parametric study was carried out to obtain near-optimized distribution of ceramic particles through the vessel thickness that results in maximum residual stresses in an autofrettaged functionally graded composite vessel. Selected finite element results were also presented to establish the validity of the X-VMP method.

1. Introduction

Autofrettage is a process in which compressive residual stresses are induced in a vessel by applying and removing an internal pressure that is well beyond the vessel normal service pressure [1–5]. During the loading phase, a significant part of the vessel cross section undergoes plastic deformation and the unloading results in development of compressive residual stresses at the inner part and tensile residual stresses at the outer part of the vessel. The induced compressive residual stress at the inner vessel part leads to enhancement of vessel's fatigue life and load-carrying capacity [6–9], and thus longer service life under cyclic internal pressure. For metal vessels, the magnitude of the residual compressive stress that can be induced by the autofrettage process is limited by the plasticity of metal [10]. To put this in perspective, in Figs. 1 and 2, we studied the residual stresses in a thick metal vessel induced by the autofrettage process. The results were calculated using the Variable Material Properties (VMP) method developed by Jahed and Dubey [11]. In this method, the linear elastic solution of a boundary value problem is used as a basis to generate its inelastic solution. The material parameters are considered as field variables and stress distributions are obtained as a part of solution in an iterative manner. In this analysis, the vessel was divided into thin strips (i.e. cylindrical elements) over its thickness and the VMP method was used to estimate the state of stress in the vessel. We assumed that the metal has bilinear elastic–plastic response under uniaxial loading with isotropic hardening behavior during unloading. The metal has elastic modulus, $E_m = 56$ GPa, tangent modulus, $H_m = 12$ GPa, and yield stress under uniaxial loading, $\sigma_y^m = 106$ MPa – see Fig. 1A. The metal Poisson ratio, denoted by ν_m, was assumed to be equal to 0.25. The thickness and internal radius of the vessel are denoted by t and R, respectively. Fig. 1B and C shows the residual hoop and radial stresses for a vessel with $t/R = 1$, respectively, subjected to different autofrettage pressures denoted by P. For low values of autofrettage pressure, the vessel behaves elastically over most of its sectional area during the loading phase of the autofrettage process (i.e. applying the internal pressure) and thus, the residual hoop stresses are considerable only close to the inner surface (bore) of the vessel (e.g. see the results for $P = 50$ MPa in Fig. 1B). In this case, the maximum residual hoop stress is generally lower than the metal yield stress. By increasing the autofrettage pressure, plastic deformation occurs over a larger sectional area of the metal vessel during the loading phase. For $P = 100$ MPa, the results show that the outer part of the metal vessel, $x/R > 0.8$, deforms only elastically during the loading phase of the autofrettage pressure, which manifests by a sudden change in the slope of residual stress curve at $x/R \cong 0.8$. For $P = 300$ MPa, the metal vessel deforms plastically over its entire cross section during the loading phase. Note that there is very little difference between the calculated residual hoop stresses in the inner part of the metal vessel for $P = 100$ MPa and 300 MPa. The residual radial stresses are compressive through the thickness of the vessel with values that are generally much lower than the residual hoop stresses as quantified in Fig. 1C.

* Corresponding author.
E-mail address: vaziri@coe.neu.edu (A. Vaziri).

0263-8223/$ - see front matter © 2010 Elsevier Ltd. All rights reserved.
doi:10.1016/j.compstruct.2010.01.019

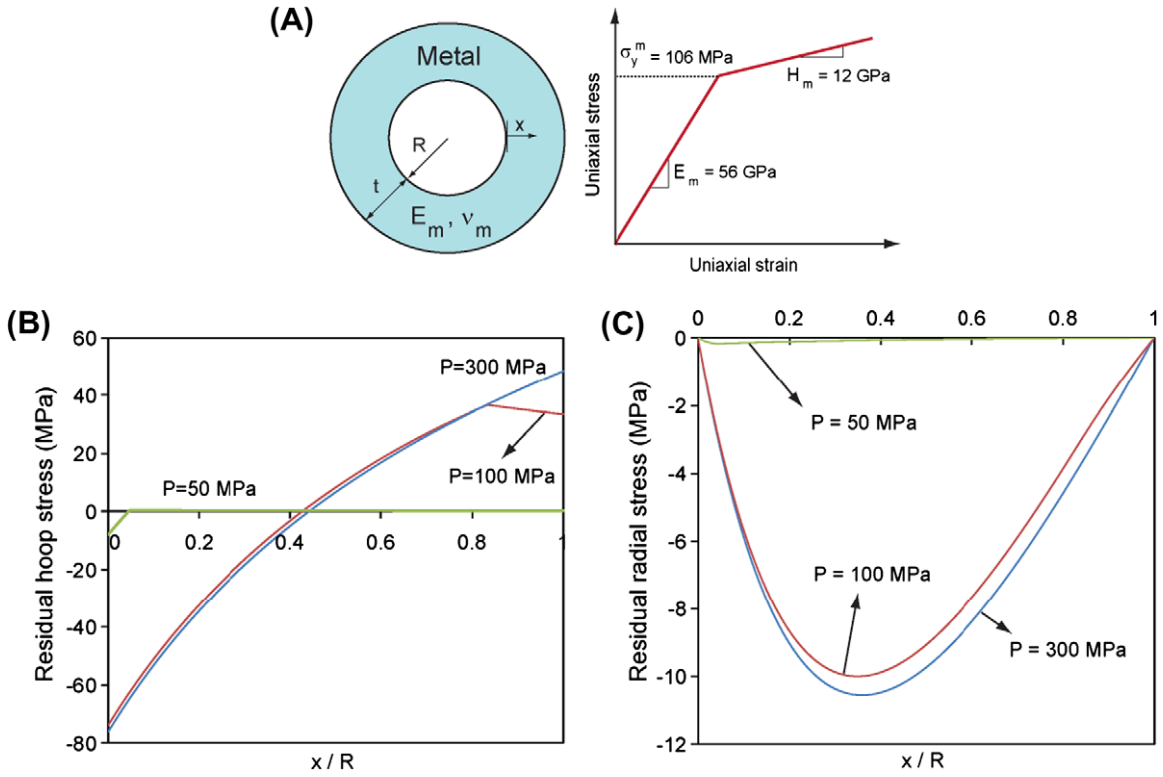

Fig. 1. Autofrettage of a metal vessel. (A) Schematic of a thick metal vessel with internal radius R and thickness t, and metal material properties. (B and C) Residual hoop and radial stresses along the thickness of a metal vessel with $t/R = 1$ for different autofrettage pressures.

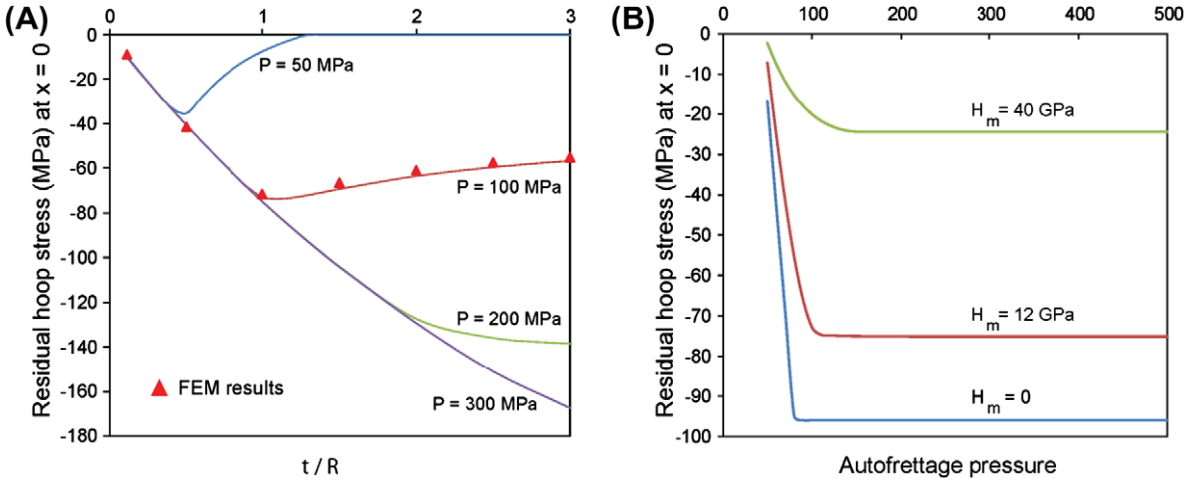

Fig. 2. (A) Residual hoop stress at the inner surface of a metal vessel versus the normalized thickness of the vessel, t/R, for different autofrettage pressures. (B) Residual hoop stress at the inner surface of a metal vessel with $t/R = 1$ versus the autofrettage pressure for different metal tangent moduli, H_m.

Fig. 2A summarizes the results of a parametric study on the induced residual hoop stresses at the inner surface of the vessel with different thickness to radius ratio. The residual hoop stress approaches zero for thin-walled vessels (i.e. small values of t/R) due to the quasi-uniform distribution of the stresses through the vessel thickness during the loading and unloading phases. For thicker vessels, the value of the residual stresses reaches its maximum at a critical t/R for each autofrettage pressure, which approximately corresponds to the thickness at which the autofrettage percent is 100% (i.e. the vessel deforms plastically over its entire cross-section area during the loading phase). For vessels thinner than the critical thickness, the residual stress at the inner surface remains constant by increasing the applied autofrettage pressure. For autofrettaged vessels with low values of autofrettage pressure (e.g. $P = 50$ MPa in Fig. 2A), there is also a maximum thickness at which the residual hoop stress in the vessel is non-zero since plastic deformation does not occur in thicker vessels during the loading phase. At a higher autofrettage pressure, a part of the vessel always undergoes plastic deformation during the loading phase, leading to non-zero residual stresses after unloading. The residual stress at the inner surface of the vessel, first increases by increasing the vessel thickness till the thickness reaches the critical thickness value discussed above and then decreases by increasing the vessel thickness, approaching zero as $t/R \to \infty$. A complementary set of calculations was carried out to study the role of metal hardening characteristics on the induced residual stresses in an autofrettaged

metal vessel. The results of this study are summarized in Fig. 2B, which shows that the maximum inducible residual stress is remarkably decreased and is achievable at a higher autofrettage pressure as the metal tangent modulus increases.

The above discussion clearly highlights a key limitation of autofrettaged metal vessels, which is its constriction by metal plasticity behavior. Several techniques have been proposed to address this limitation. Mughrabi et al. [12] and Feng et al. [13] proposed low-temperature autofrettage of vessels and showed that higher compressive hoop residual stress can be achieved by this technique. The key reason is that the stiffness and yield strength of metal are higher at low temperature and the thermal strains accumulated during warm up to room temperature elevates the compressive stresses induced in the vessel. Combination of autofrettage and shrink fit [14–16] and re-autofrettage [17,18] have been also used to enhance the performance of vessels.

In this paper, we explore an alternative approach from the materials perspective. We considered two different vessels made of layered and functionally graded composites and studied the residual stresses in these vessels by the autofrettage process using a numerical method that is an extension of the Variable Material Properties (X-VMP). The developed method, which is introduced in our previous paper [19] and discussed in details in Section 2, allows us to analyze axisymmetric structures made of materials with varying elastic and plastic properties with high fidelity and efficiency. Our work complements the previous studies on axisymmetric functionally graded structures, including rotating disks with variable thickness [20], hollow cylinders subjected to internal pressure and/or tangential tractions on the outer surface [21], brake disks [22], and pressurized disks and cylinders [23].

Throughout this paper, the results based on finite element analysis are also provided to establish the validity of the X-VMP method using commercially available software, ABAQUS. The results for the autofrettage of metal–ceramic layered composite vessels, including bilayer and multi-layered vessels are presented in Section 3. In Section 4, the autofrettage of functionally graded ceramic-reinforced composite vessels is investigated and a parametric study is performed to obtain the near-optimized distribution of ceramic particles, which results in a maximum residual stress at the inner surface of the vessel. Conclusions are drawn in Section 5.

2. Extended Variable Material Properties (X-VMP)

In this method, the structure (in this case a thick vessel) is divided into infinitesimal elements, which are assumed to be made of a homogenous material. For the vessel shown in Fig. 3, the material behavior of an element located at a distance x from the inner radius of the vessel is characterized with its elastic modulus and Poisson ratio, denoted by $E(x)$ and $v(x)$, respectively, and a curve that represents the plastic behavior of the element. The component of strain tensor for this element, ε_{ij}, is the summation of the elastic part, ε^e_{ij} and the plastic part, ε^p_{ij}. The elastic part is given by:

$$\varepsilon^e_{ij} = \frac{1+v(x)}{E(x)}\sigma_{ij} - \frac{v(x)}{E(x)}\sigma_{kk}\delta_{ij} \tag{1}$$

where δ_{ij} is the Kronecker delta and the plastic part of the strain is given by Hencky's total deformation equation, $\varepsilon^p_{ij} = \phi(x)s_{ij}$, where $s_{ij} = \sigma_{ij} - \frac{1}{3}\sigma_{kk}\delta_{ij}$ is the deviatoric stress, and ϕ is a scalar function given by $\phi = \frac{3}{2}\frac{\bar{\varepsilon}^p}{\sigma_{eq}}$, where $\bar{\varepsilon}^p$ and σ_{eq} are the equivalent plastic strain and equivalent stress, respectively. Considering the above relationships, the total strain in the element can be written as,

$$\varepsilon_{ij} = \left(\frac{1+v(x)}{E(x)} + \phi_{(x)}\right)\sigma_{ij} - \left(\frac{v(x)}{E(x)} + \frac{1}{3}\phi(x)\right)\sigma_{kk}\delta_{ij} \tag{2}$$

Following the VMP method, we assume *an elastic element* located at x, with an effective elastic modulus, $E_{eff}(x)$, and an effective Poisson ratio, $v_{eff}(x)$, that has elastic strain components equal to the total strain components of the elasto-plastic element presented in Eq. (2). The component of strain tensor in this equivalent elastic element is,

$$\varepsilon^*_{ij} = \frac{1+v_{eff}(x)}{E_{eff}(x)}\sigma_{ij} - \frac{v_{eff}(x)}{E_{eff}(x)}\sigma_{kk}\delta_{ij} \tag{3}$$

Comparing Eqs. (2) and (3), the following relationships can be obtained:

$$E_{eff}(x) = \frac{3E(x)}{3+2E(x)\phi(x)}$$
$$v_{eff}(x) = \frac{3v(x)+E(x)\phi(x)}{3+2E(x)\phi(x)} \tag{4}$$

Eliminating $\phi(x)$ from the above equations gives:

$$v_{eff}(x) = \frac{E_{eff}(x)(2v(x)-1)+E(x)}{2E(x)} \tag{5}$$

To obtain the stress distribution, first the state of stress in the vessel is evaluated using theory of elasticity by assuming $E_{eff}(x) = E(x)$ and $v_{eff}(x) = v(x)$ and considering that all elements satisfy the requirements of equilibrium and compatibility at their boundaries (i.e. interface with adjacent elements). Once the state of stress in each layer is obtained, $E_{eff}(x)$ is updated for each element based on the calculated equivalent (von Mises) stress, σ_{eq}, using the projection method [11]. In this method, the equivalent strain is obtained from the calculated equivalent stress using $\varepsilon_{eq} = C^{-1}(\sigma_{eq})$, where $\sigma_{eq} = C(\varepsilon_{eq})$ is the stress–strain curve for the material located at a distance x. Then, the value of the effective elastic modulus is updated as $E_{eff} = \frac{\sigma_{eq}}{\varepsilon_{eq}}$. The effective Poisson ratio for each element, $v_{eff}(x)$, is obtained using Eq. (5). In the next step, the state of stress in each element is re-calculated using the updated values of effective elastic modulus and effective Poisson ratio. This procedure is continued until the convergence is achieved. The numerical procedure gives a close estimate of the elasto-plastic stresses in the structure.

For the case of a pressurized hollow cylinder, the governing elastic equations – known as Lamé's equations – provide the elastic solution in each step for an equivalent vessel [24]. According to Lamé's equations, for each thin strip located at x, the inside and outside displacements, u_x and u_{x+dx}, are related to the inside and outside pressures, p_x and p_{x+dx}, by the following relations:

$$\begin{bmatrix} C_{11,x} & C_{12,x} \\ C_{21,x} & C_{22} \end{bmatrix}^{-1} \begin{Bmatrix} u_x \\ u_{x+dx} \end{Bmatrix} = \begin{Bmatrix} p_x \\ p_{x+dx} \end{Bmatrix} \tag{6}$$

where for the plane strain condition:

$$C_{11,x} = \frac{1+v_{eff}(x)}{E_{eff}(x)}\frac{(R+x)^3}{(R+x+dx)^2-(R+x)^2} \times \left(1-2v_{eff}(x)+\frac{(R+x+dx)^2}{(R+x)^2}\right)$$
$$C_{12,x} = -2\frac{(1+v^2_{eff}(x))}{E_{eff}(x)}\frac{(R+x)(R+x+dx)^2}{(R+x+dx)^2-(R+x)^2}$$
$$C_{21,x} = 2\frac{(1-v^2_{eff}(x))}{E_{eff}(x)}\frac{(R+x)(R+x+dx)^2}{(R+x+dx)^2-(R+x)^2}$$
$$C_{22,x} = -\frac{1+v_{eff}(x)}{E_{eff}(x)}\frac{(R+x+dx)^3}{(R+x+dx)^2-(R+x)^2} \times \left(1-2v_{eff}(x)+\frac{(R+x)^2}{(R+x+dx)^2}\right) \tag{7}$$

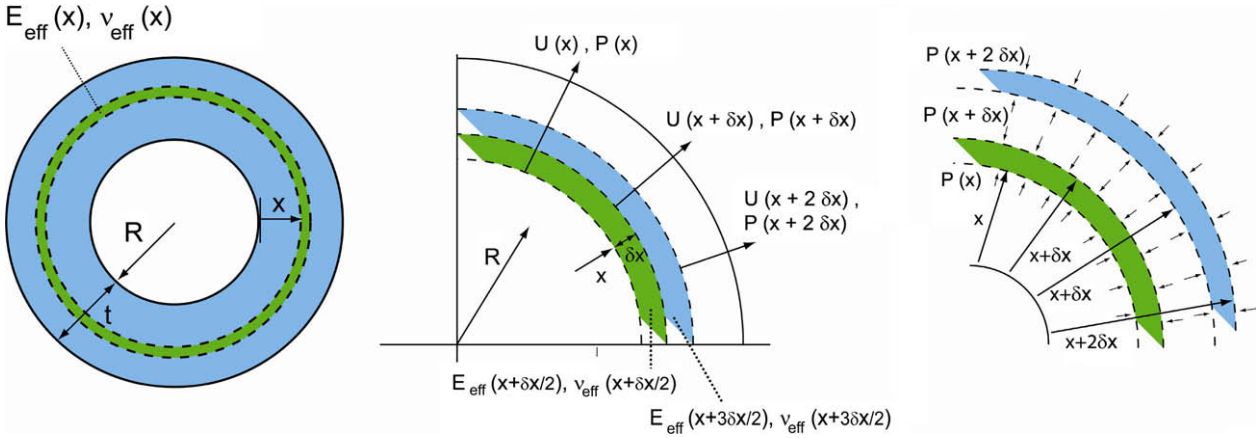

Fig. 3. Schematic of a vessel with varying material property. The figure shows the displacements and pressures interacting between adjacent thin elements as the vessel is subjected to an internal pressure.

where R and x are the inner vessel radius and the distance of the element from the inner surface of the vessel, respectively – see Fig. 3A. The governing equation is obtained by assembling Eq. (6) for all elements with x ranging from 0 to t. Solving this set of equations gives the displacement field in the vessel induced by the applied pressure. Once the displacement field is obtained, the radial and hoop stresses can be determined from the Lamé equations for the hollow cylinder, by using Eqs. (6) and (7).

The autofrettage problem also requires finding the unloading solution of the FGM vessels. The unloading solution is analogous to loading except that each element has a specific nonlinear unloading behavior which depends on the element's equivalent stress at the onset of unloading and also the material hardening behavior (e.g. isotropic hardening or kinematic hardening). It should be noted, since the material in each element undergoes plastic deformation in the loading phase, an updated stress–strain curve should be considered for each layer in the unloading phase. Once the loading and unloading stresses are calculated based on the method outlined above, the residual stress field can be estimated by superposing the loading and unloading stress solutions. In the X-VMP results presented in the following sections, we assumed that the metal–ceramic composite is locally isotropic, yields

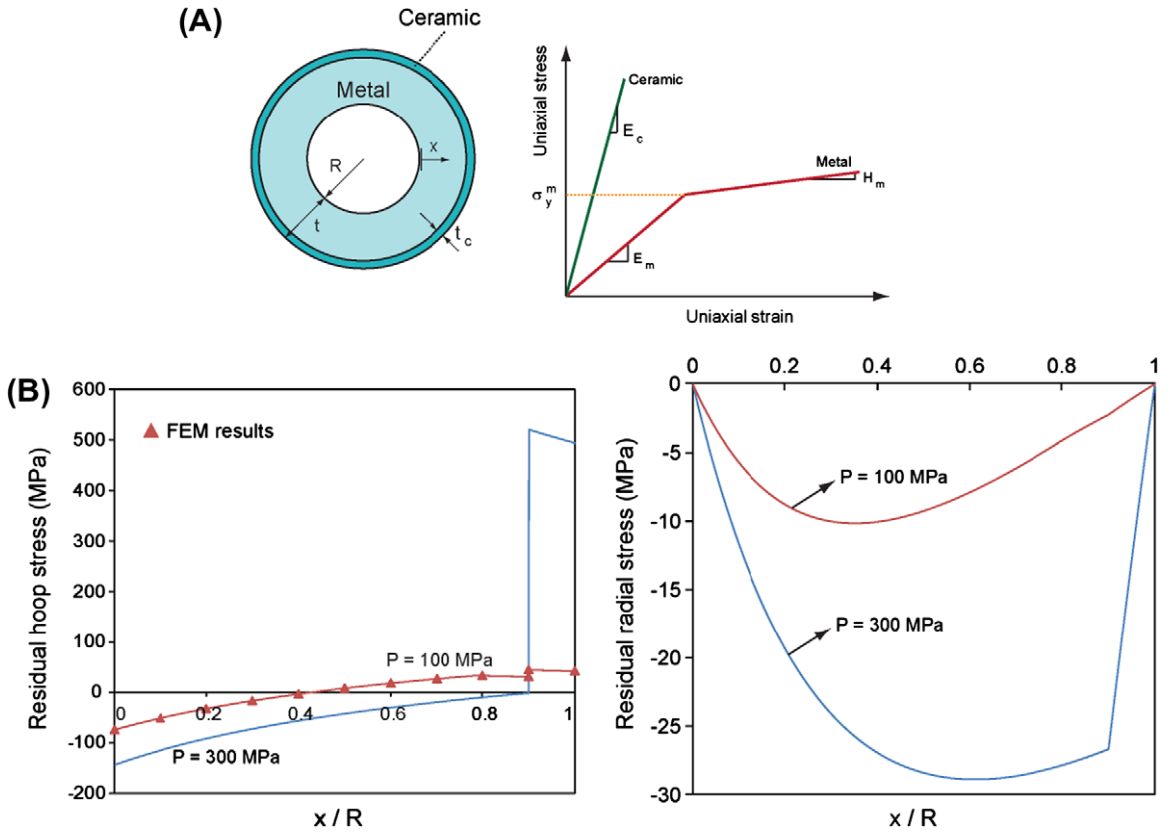

Fig. 4. Autofrettage of a bilayer metal–ceramic vessel. (A) Schematic of a bilayer vessel and the corresponding stress strain curves of metal and ceramic. (B) Residual hoop and radial stresses through the thickness of an autofrettaged vessel with for $P = 100$ and 300 MPa. In this set of results $t/R = 1$and $t_c/t = 0.1$.

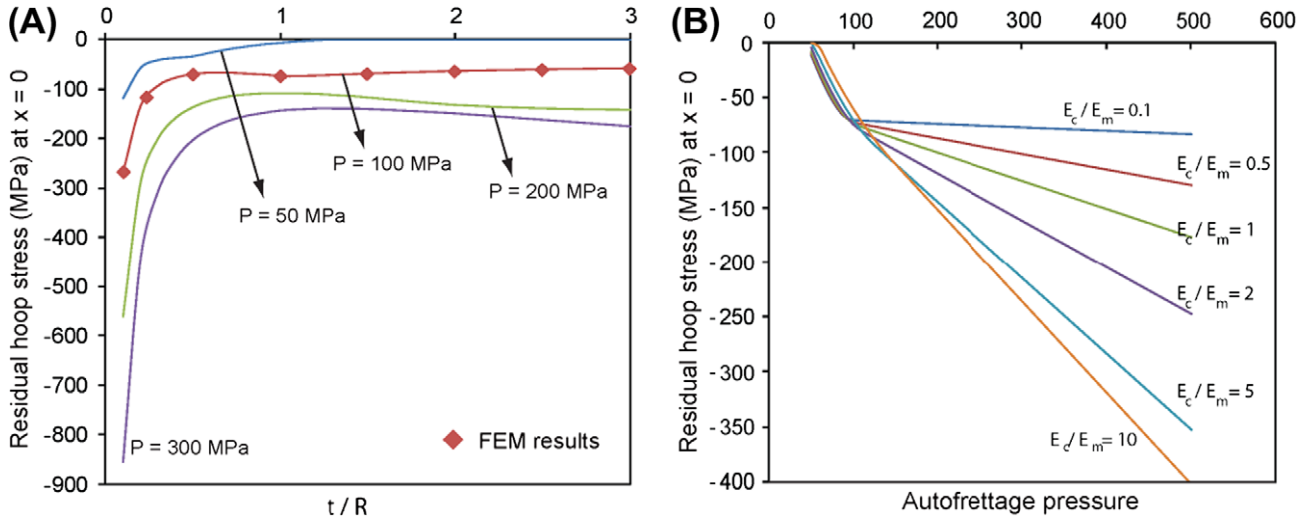

Fig. 5. (A) Residual hoop stress at the inner surface of a bilayer vessel with $t_c/t = 0.1$ versus the normalized thickness of the vessel, t/R, for different autofrettage pressures. (B) Residual hoop stress at the inner surface of the vessel with $t/R = 1$ and $t_c/t = 0.1$ versus the autofrettage pressure for different values of E_c/E_m.

according to the von Mises criterion and follows isotropic hardening behavior during unloading.

3. Autofrettage of metal–ceramic layered composite vessels

We considered three different configurations of multi-layer metal–ceramic vessels: (1) bilayer vessel consisting of a ceramic layer attached to the outer surface of a metal layer, (2) trilayer vessel, where the middle layer is ceramic and the inner and outer layers are metal and (3) layered vessels consisting of two ceramic layers and two metal layers, with one ceramic layer always located at the outer surface of the vessel. First, we discuss the results for a bilayer vessel with internal radius, R, and thickness, t, where a ceramic layer with thickness t_c is bonded to the outer surface of a metal layer (with thickness $t–t_c$) – see Fig. 4A. This configuration is particularly of interest since the ceramic layer at the outer surface of the vessel may provide enhanced oxidation, corrosion and wear resistance and thermal insulation [25–32]. In the results presented in this section, the metal layer was assumed to have bilinear elastic–plastic behavior with material constants as given in Fig. 1. The ceramic was assumed linear elastic with elastic modulus that varied systematically between 5.6 GPa and 560 GPa (i.e. $0.1 < E_c/E_m < 10$, where E_c denotes the ceramic elastic modulus) with constant Poisson ratio 0.25.

The distribution of residual hoop and radial stresses along the thickness of a bilayer vessel with $t/R = 1$ and $t_c/t = 0.1$ is shown in Fig. 4B for $P = 100$ MPa and 300 MPa. Finite element results for the residual hoop stress at $P = 100$ MPa are also plotted which shows a good agreement with the numerical results obtained based on the X-VMP method. The finite element models were meshed using two-dimensional, 8-node quadrilateral elements and mesh sensitivity analysis was performed to assure that the results are not sensitive to the element size. ABAQUS standard solver with the plane strain and small deformation condition was used to simulate the response of the vessel during the autofrettage process. The results for the bilayer vessel subjected to a pressure 100 MPa is not considerably different from the results for a metal vessel counterpart presented in Fig. 1B. However, a significant difference exists between the residual stresses induced by the autofrettage in the metal, and bilayer vessels at a pressure 300 MPa. First, the compressive residual hoop stress at the inner surface is much higher in the bilayer vessel compared to its metal vessel counterpart. Second, the compressive residual hoop stress is induced over a larger depth of the bilayer vessel compared to the metal vessel (i.e. for the bilayer vessel, the whole metal layer is under compressive residual hoop stresses, while for the metal vessel the compressive residual hoop stress is induced only at $x/R < 0.45$). The residual radial stresses at $P = 300$ MPa are also much higher for this configuration compared to a metal vessel counterpart.

The effect of vessel thickness to inner radius ratio on the value of residual hoop stresses induced at the inner surface of an autofrettaged vessel is presented in Fig. 5A for various autofrettage pressures. In this set of results, the ratio of the ceramic layer thickness to vessel thickness, t_c/t, is kept constant and equal to 0.1. The finite element results are also provided for the autofrettage pressure of 100 MPa, which again shows a good agreement with the results obtained using X-VMP method. Unlike uniform metallic vessels, decreasing the overall thickness of vessel results in an increase in the induced compressive residual hoop stress, Fig. 5A. Finally, we studied the role of the relative stiffness of the ceramic to metal layer, E_c/E_m, on induced residual hoop stresses at the inner surface of a bilayer vessel, Fig. 5B. By increasing the relative stiffness of ceramic layer, the residual hoop stress increases significantly for autofrettage pressures larger than approximately 100 MPa. Also, unlike metal vessels, bilayer vessels show no limit in the induced residual hoop stress as the autofrettage pressure is increased.

In the next step, we considered a trilayer metal–ceramic vessel, where one ceramic layer with thickness t_c is located inside the vessel at distance x_c from the vessel inner surface, as shown schematically in Fig. 6A. Fig. 6B shows the distribution of residual hoop and radial stresses along the thickness of a vessel with $t/R = 1$ and $t_c/t = 0.1$, for $P = 300$ MPa. The residual hoop stress at the inner surface of the vessel is higher for vessels with the ceramic layer closer to the vessel inner surface. In addition, the residual stresses in the ceramic layer are always tensile since the structure expands during loading and the elastic ceramic layer cannot return to its original size after unloading. The residual radial stress in the inner metal layer is compressive and changes abruptly in the ceramic layer. Depending on the location of the ceramic layer, the residual radial stress in the outer metal layer could be tensile, compressive or changes from tensile at the outer surface of the ceramic layer to compressive, as quantified in Fig. 6B for several different values of x_c/t. We have confirmed

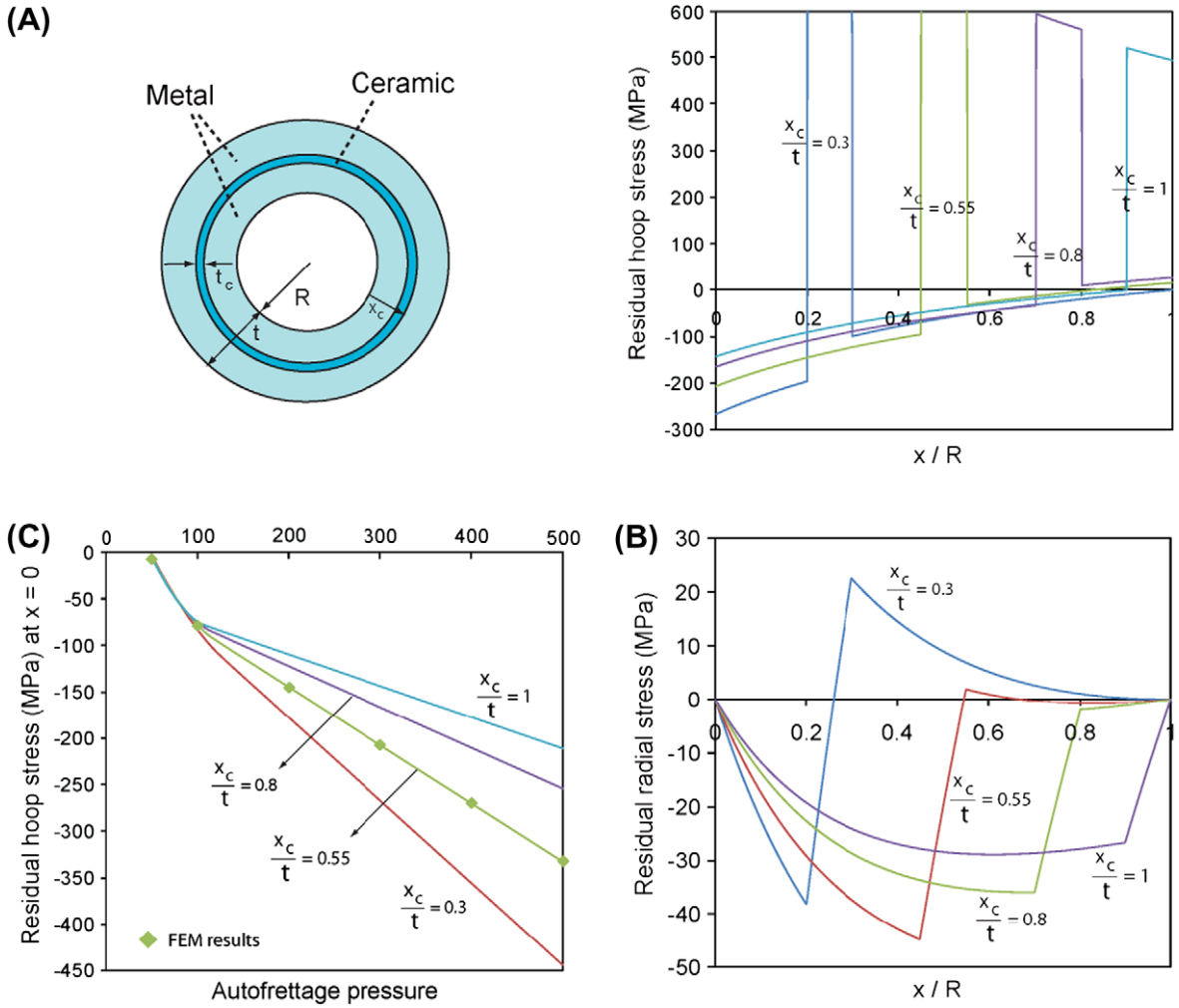

Fig. 6. Autofrettage of trilayer metal–ceramic vessel. (A) Schematic of a metal–ceramic–metal vessel, where t_c is the thickness of the ceramic layer and x_c is the distance of the outer surface of the ceramic layer from the inner radius of the vessel. (B) Residual hoop and radial stresses through the thickness of an autofrettaged vessel for $P = 300$ MPa and different x_c/t. (C) Residual hoop stress at the inner surface of the vessel versus the autofrettage pressure for different x_c/t. In this set of results $t/R = 1$ and $t_c/t = 0.1$.

these results using finite element analysis – the results are not shown here for the sake of brevity. Fig. 6C shows the dependence of the residual hoop stress at the inner surface of the vessel on the autofrettage pressure for the trilayer vessel configuration. The results are plotted for several values of x_c/t. One set of finite element results for $x_c/t = 0.55$ is also provided for validation. Similar to the case of bilayer vessels, trilayer vessels show no limit in the induced residual hoop stress by increasing the autofrettage pressure.

Finally, we considered a layered metal–ceramic vessel consisting of two metal layers and two ceramic layers. In the calculation performed for this configuration, one ceramic layer is always located at the outer surface of the vessel, while the other ceramic layer is located at a distance x_c from the vessel inner surface, as shown schematically in Fig. 7A. The calculations carried out in Fig. 6 for trilayer vessels are repeated for this configuration and the results are summarized in Fig. 7B and C. The results are consistent with the results of the trilayer vessels: First, by moving the inner ceramic layer towards the inner bore of the vessel, the hoop residual stress at the inner surface of the vessel increases. Second, there is no limit in the induced residual hoop stress by increasing the autofrettage pressure. The distribution of the residual radial stress is also qualitatively similar to the results obtained from the analysis of trilayer vessels.

For the layered composite vessel configurations studied, the ceramic layer is subjected to a significant residual tensile stress through its thickness. This is clearly the key disadvantage of this configuration since ceramics are generally brittle and high residual tensile stresses could lead to immature failure of the ceramic layer. In Section 4, we explore the residual stresses in an autofrettaged vessel made of functionally graded metal–ceramic composite, which indeed eliminates the shortcomings outlined above for bilayer, and in general layered, composite vessels.

4. Autofrettage of functionally graded composite vessels

FGMs, while offering the advantages of composites, avoid the negative effects of abrupt changes in the material constituent due to the monotonous variation in their composition. In our previous study, we demonstrated the potential application of FGM for designing autofrettaged vessels [19]. Our work suggests that reinforcement of metal vessels with ceramic particles with an increasing volume fraction through its radius – even in small quantities – increases the compressive stresses induced by the autofrettage process. The calculated residual stresses also do not exhibit the abrupt change observed in the layered metal–ceramic composite vessels discussed in Section 3. Here, we extend our previous study

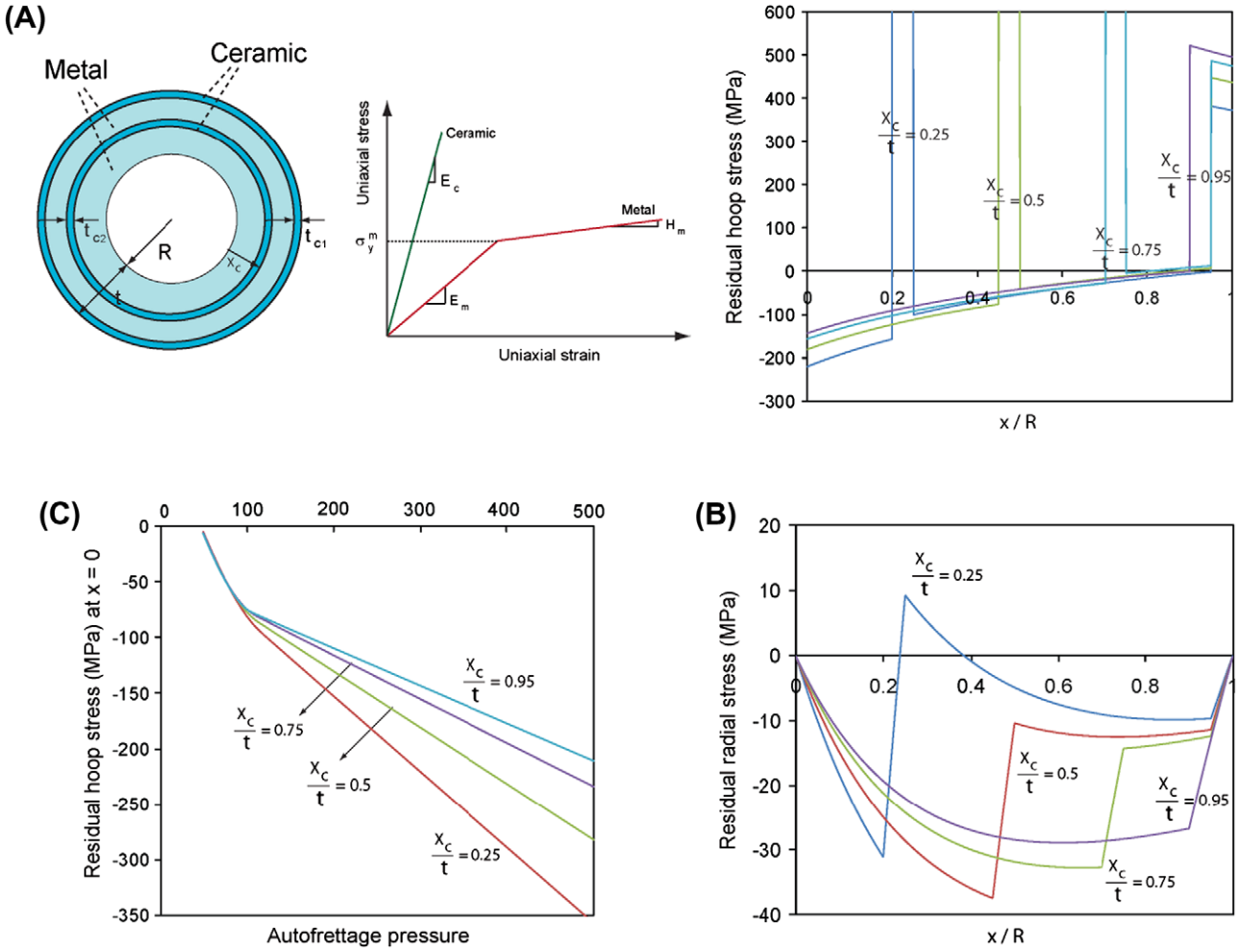

Fig. 7. Autofrettage of a multi-layer metal–ceramic composite vessel. (A) Schematic of the composite vessel, where t_{c2} is the thickness of the ceramic layer located at x_c and t_{c1} is the thickness of the ceramic layer bonded to the outer surface of the vessel. (B) Residual hoop and radial stresses through the thickness of an autofrettaged vessel for $P = 300$ MPa and different x_c/t. (C) Residual hoop stress at the inner surface of the vessel versus the autofrettage pressure for different x_c/t. In this set of results, $t/R = 1$ and $t_{c1}/t = t_{c2}/t = 0.05$.

by carrying out parametric studies to highlight the role of ceramic particle strength and spatial distribution on the residual stresses in the autofrettaged FGM vessel and to also achieve the near-optimized ceramic particle distribution that leads to maximum induced residual stress at the inner surface of the FGM vessel. Similar to Section 3, we assume that the metal has bilinear elastic–plastic behavior and the ceramic has linear elastic behavior with material constants presented in Section 3. The elastic modulus of the metal–ceramic composite, E_{comp}, the overall flow strength of the composite corresponding to the onset of plastic yielding, σ_y^{comp} and the tangent modulus of the composite, H_{comp}, which represents its strain hardening behavior, can be calculated using the modified rule of mixture for composites [33] – see Fig. 8A.

$$E_{comp} = \left[(1-f)\left(\frac{q+E_c}{q+E_m}\right)+f\right]^{-1} * \left[(1-f)E_m\left(\frac{q+E_c}{q+E_m}\right)+fE_c\right]$$
$$\sigma_y^{comp} = \sigma_y^m\left[(1-f)+\left(\frac{q+E_m}{q+E_c}\right)\cdot\frac{E_c}{E_m}\cdot f\right]$$
$$H_{comp} = \left[(1-f)\left(\frac{q+E_c}{q+H_m}\right)+f\right]^{-1} * \left[(1-f)H_m\left(\frac{q+E_c}{q+H_m}\right)+fE_c\right] \quad (8)$$

where f denotes the volume fraction of the ceramic particles. Finding the composite material constants required having parameter q, which is the ratio of stress to strain transfer that defines the metal/ceramic composite behavior [33]. In all the results presented here, the ratio $\frac{q}{E_c}$ is taken as 0.86 based on the micro-indentation experiments by Gu et al. [34]. In this study, the ceramic particle reinforcement is taken to be constant in the circumferential direction and to have a volume fraction that varies from 0 at the inner surface to f_0 at the outer surface according to, $f(x) = f_0\left(\frac{x}{t}\right)$, where n is the reinforcement distribution exponent. In this case, $f_0 = 0$ denotes a metal vessel and $n = 0$ denotes uniformly-reinforced metal–ceramic vessel. The average volume fraction of the ceramic is $f_{ave} = 2f_0\ (R/(n+1)+t/(n+2))/(t+2R)$.

In Fig. 8B, the distribution of residual hoop stress through the thickness of FGM vessels with different reinforcement coefficients, f_0, are plotted. In this set of results, the average volume fraction of the ceramic is kept constant as $f_{ave} = 0.4$ (i.e. the vessels have different reinforcement distribution exponents). Finite element results for the case of $f_0 = 1$ is also plotted which is in good agreement with the numerical solution. For modeling the FGM vessels, the vessel was divided to forty circular layers with equal thickness. It was assumed that each layer has uniform elastic modulus, tangent modulus and yield stress, which were calculated at the center of the layer using Eq. (8). We checked that increasing the number of layers through the thickness of the vessel does not yield any considerable change in the results. Similar to the

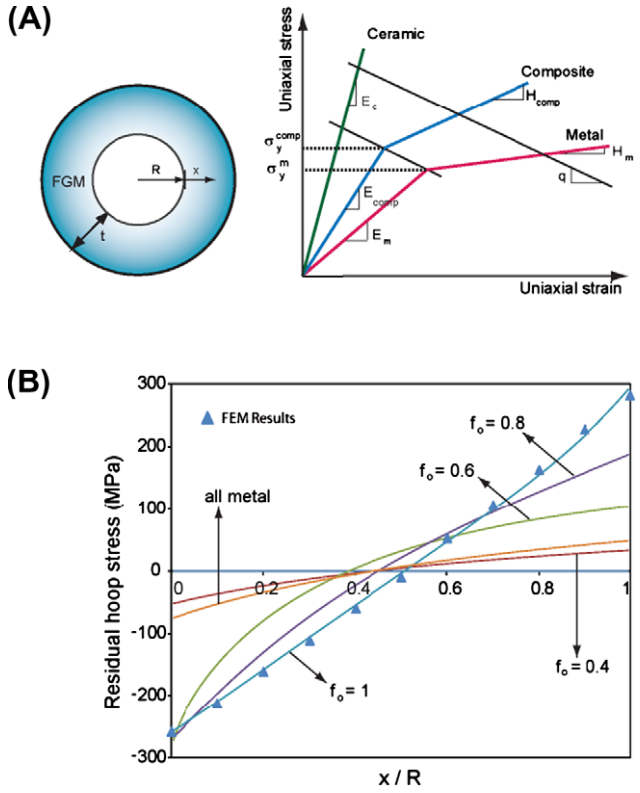

Fig. 8. Autofrettage of a functionally graded ceramic-reinforced metal composite vessel. (A) Schematic of the vessel and the modified rule of mixtures used to estimate the behavior of ceramic-reinforced metal composite based on the ceramic volume fraction in composite. (B) Residual hoop stress in composite vessels with different ceramic distributions coefficient, f_0, but constant ceramic average volume fraction $f_{ave} = 0.4$ and also in an all metal vessel are shown. In this set of results, $t/R = 1$ and $P = 300$ MPa.

models created for layered composite vessels, the models were meshed using two-dimensional, 8-node quadrilateral elements and mesh sensitivity analysis was performed to assure that the results are not sensitive to the element size.

The results show that the induced residual stress at the inner surface of the uniformly-reinforced vessel is lower than the residual stress in the autofrettaged metal vessel counterpart. However, non-uniform reinforcement of the metal vessel with ceramic particles could lead to remarkably higher residual stresses as quantified in Fig. 8B for FGM vessels with $f_0 = 0.6$, 0.8 and 1. In this set of calculations, the residual stress at the inner surface of the FGM cylinder with $f_0 \geqslant 0.6$ is almost constant, however, the distribution of the residual stress through vessel thickness is sensitive to f_0 (note that the average volume fraction is kept constant). In Fig. 9A, we have expanded these results for vessels with different ceramic particle distributions. The residual hoop stress at $x = 0$ (inner surface) is plotted against the ceramic average volume fraction, f_{ave}, for the autofrettage pressure of 300 MPa. For each set of calculations, f_0 is kept constant and the ceramic average volume fraction is increased from 0 to f_0 (i.e. $0 < f_{ave} \leqslant f_0$, where $f_{ave} = f_0$ corresponds to a uniform ceramic particle distribution). The results show different distributions of ceramic particles that could lead to maximum induced residual stress at the vessel inner surface. For example, for $f_0 = 1$, the maximum achievable residual stress at the inner surface of the vessel is 318 MPa, which is achieved for $f_{ave} = 0.65$ (which corresponds to the distribution exponent, $n = 0.67$). In general, increasing the ceramic particle volume fraction at the outer surface of the vessel elevates the maximum achievable residual stress. Fig. 9B shows the maximum achievable residual stress at the vessel inner surface normalized by the autofrettage pressure versus f_{ave} for different autofrettage pressures. Fig. 9C shows the optimum ceramic particle distributions for each autofrettage pressure that leads to the highest value of residual compressive stress at the inner surface of the vessel. For high values of ceramic average volume fraction, the optimum distribution is achieved, when the outer surface has no metal content and is fully made of ceramic (i.e. $f_0 = 1$). This optimum distribution is the same for autofrettage pressure of 200 MPa and higher and is achieved at $f_0^{opt} \approx 1.66\, f_{ave}$ for $f_{ave} < 0.6$ and at $f_0^{opt} = 1$ for higher values of f_{ave}. Finally, In Fig. 10, we investigated the effect of ceramic particles stiffness on the maximum achievable compressive residual stress in an autofrettaged vessel. Fig. 10A shows the maximum achievable residual stress calculated for various ceramic particles stiffness and average volume fractions for $P = 300$ MPa. The range of ceramic stiffness considered in this study is $0.1 \leqslant E_c/E_m \leqslant 10$. The near-optimized distribution of ceramic particles depends on the ceramic stiffness as quantified in Fig. 10B for $P = 300$ MPa. The exception is for high values of ceramic average volume fraction, where the optimum distribution is $f_0^{opt} = 1$, independent of the ceramic stiffness.

5. Conclusions

In this paper, we investigated the residual stresses induced by autofrettage process in layered and functionally graded composite vessels. The calculations were carried out using X-VMP method and validated in several cases using finite element calculations. Our study showed that the induced residual stress at the inner surface of composite vessels with above configurations could reach much higher values compared to a metal vessel counterpart depending on the properties of composite constituents. However, it should be emphasized that only a theoretical model for evaluation of residual stresses was offered here and further studies are needed to effectively evaluate the residual stresses induced in the vessel during the autofrettage process and its impact and relationship with the vessel reliability and service life. The provided theoretical model does not account for the failure of the material, and thus, the results are valid only prior to material constituents' failure. Many ceramics undergo brittle failure at small strains and thus, the provided results and conclusions might only be valid for internal pressures lower than the values studied here. Another concern for layered ceramics is the layer interface strength and failure, which is not accounted in the current theoretical study. As discussed, the uncertainties and failure concerns associated with the layered composites are avoided by using functionally graded composites. However, the addition of the ceramic content in the autofrettage vessel may result in new and unpredictable failure modes – and thus, further studies are required to validate the key conclusions of the this investigation.

A parametric study was also carried out in this article to find the optimized ceramic particle distribution that produces the maximum compressive residual stresses at the inner bore. The near-optimized configurations of composite vessels were presented for several cases and insight was provided about the relationship between ceramic particle distribution and the induced residual stresses in an autofrettage process. Several techniques, such as powder processing [35–36], thermal spraying [37] and physical and chemical vapor deposition [38], have been developed for fabricating various functionally graded materials and their applicability are demonstrated for several cases. However, the lack of robust techniques for manufacturing these novel materials has decelerated their technological applications in the last decade and imposes a fundamental challenge to the materials community.

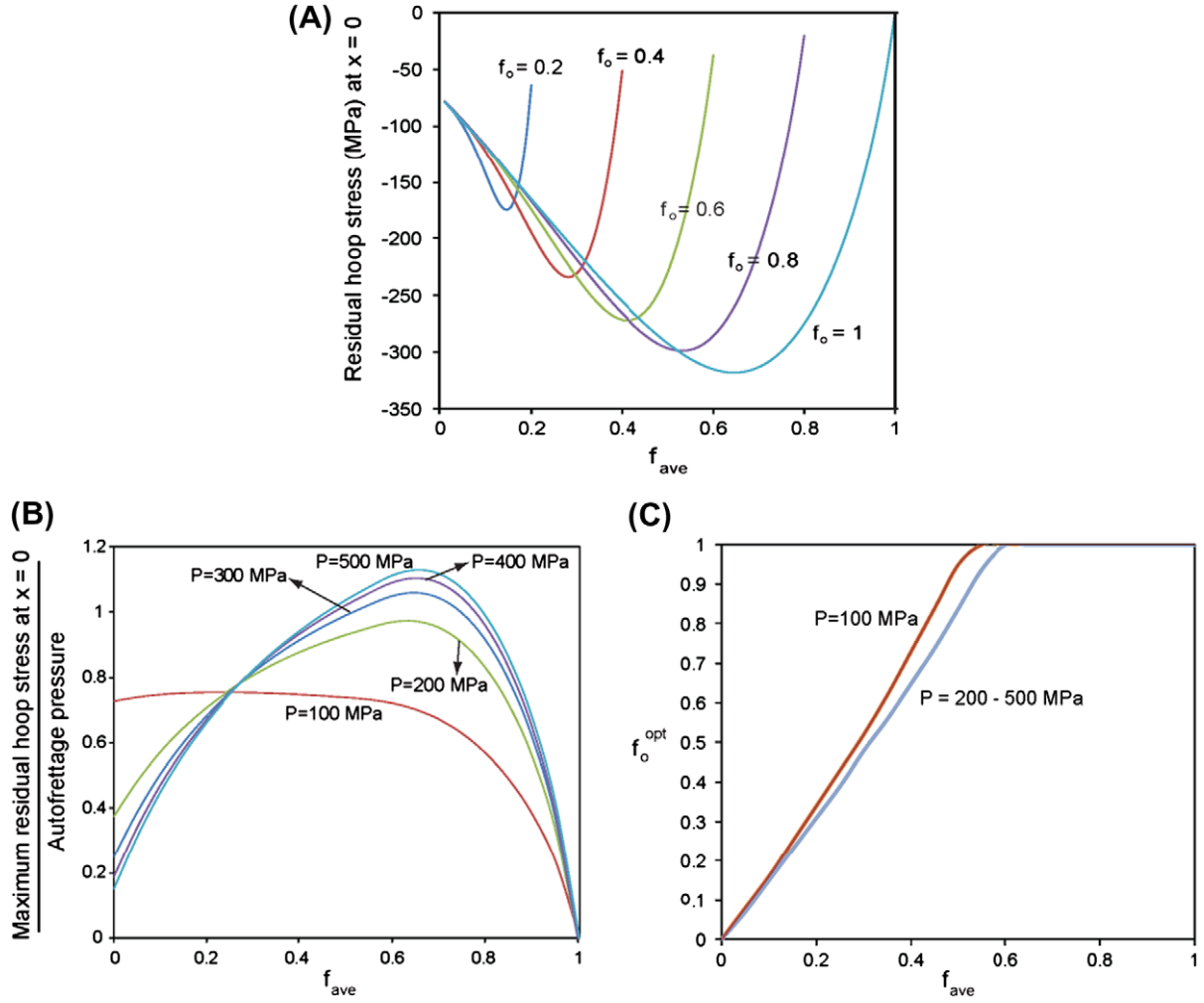

Fig. 9. Optimization of a functionally graded ceramic-reinforced metal composite vessel. (A) Residual hoop stress at inner surface of the vessel versus the ceramic average volume fraction, f_{ave}, for different reinforcement distribution coefficients, f_0. Autofrettage pressure is $P = 300$ MPa. (B) Maximum achievable residual stress at the vessel inner surface normalized by the autofrettage pressure versus the ceramic average volume fraction for different autofrettage pressures. (C) Optimum ceramic volume fraction coefficient versus the ceramic average volume fraction for different autofrettage pressures.

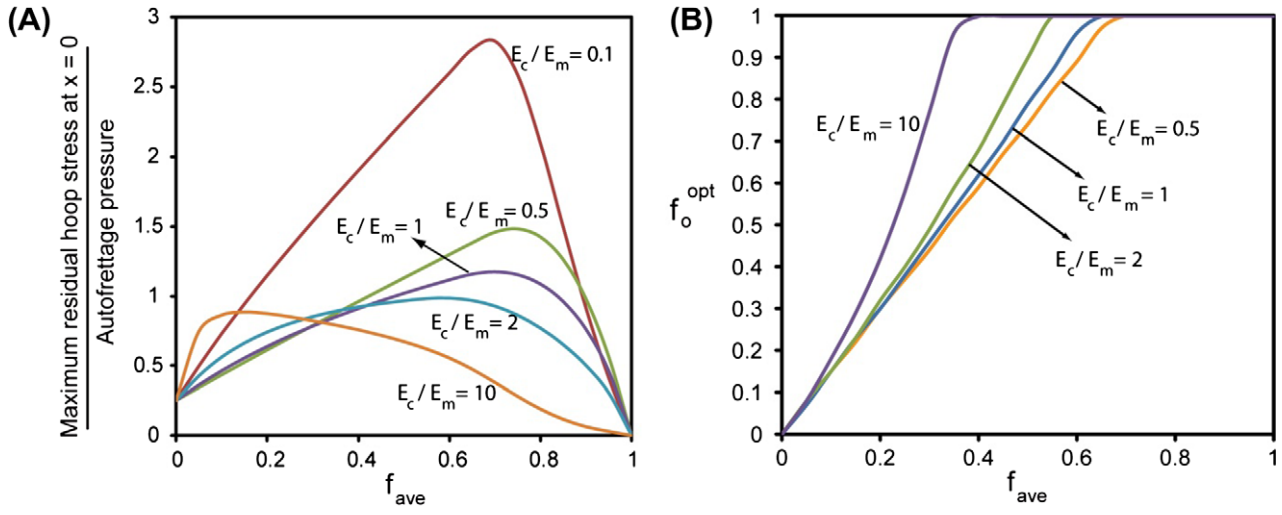

Fig. 10. Role of ceramic stiffness. (A) Maximum achievable residual stress at the vessel inner surface normalized by the autofrettage pressure versus the ceramic average volume fraction for different ceramic to metal stiffness ratios. (B) Optimum ceramic distributions, which results in a maximum residual stress at the inner surface of the vessel for different ceramic to metal stiffness ratios.

Acknowledgment

This work was supported by the Department of Mechanical and Industrial Engineering at Northeastern University.

References

[1] Farrahi GH, Hosseinian E, Assempour A. General variable material property formulation for the solution of autofrettaged thick-walled tubes with constant axial strains. ASME Int J Pressure Vessel Technol 2008;13:041209–15.
[2] Manning WRD, Labrow S. High pressure engineering. CRC Press; 1971.
[3] Chen PCT. Stress and deformation analysis of autofrettaged high pressure vessels, 110. ASME United Engineering Center; 1986. p. 61–7 [ASME special publication].
[4] Pindera MJ, Arnold SM, Aboudi J, Hui D. Use of composites in functionally graded materials. Compos Eng 1994;4:1–145.
[5] Pindera MJ, Aboudi J, Arnold SM, Jones WF. Use of composites in multi-phased and functionally graded materials. Compos Eng 1995;5:743–974.
[6] Parker AP, Underwood JH. Influence of the bauschinger effect on residual stress and fatigue lifetimes in autofrettaged thick-walled cylinders. Fatigue Fract Mech 1997;29:1814–45.
[7] Webster GA, Ezeilo AN. Residual stress distributions and their influence on fatigue lifetimes. Int J Fatigue 2001;23:S375–83.
[8] Rees DWA. The fatigue life of thick-walled autofrettaged cylinders with closed ends. Fract Eng Mater Struct 1991;14:51–68.
[9] Suresh S. Fatigue of materials. Cambridge University Press; 1998.
[10] Koh SK. Fatigue crack growth life of thick-walled cylinders with an external radial crack. Fatigue Fract Eng Mater Struct 1996;19:15–25.
[11] Jahed H, Dubey RN. An axisymmetric method of elastic–plastic analysis capable of predicting residual stress field. J Pressure Vessel Technol 1997;119:264–73.
[12] Mughrabi H, Donth B, Vetter G. Low-temperature autofrettage: an improved technique to enhance the fatigue resistance of thick-walled tubes against pulsating internal pressure. Fatigue Fract Eng Mater Struct 1997;20:595–604.
[13] Feng H, Mughrabi H, Donth B. Finite-element modeling of low temperature autofrettage of thick-walled tubes of the austentitic steel AISI 304 L: part I. Smooth thick-walled tubes. Model Simul Mater Sci Eng 1998;6:51–69.
[14] Parker AP. Bauschinger effect design procedures for compound tubes containing an autofrettaged layer. ASME J Pressure Vessel Technol 2001;123:203–6.
[15] Parker AP, Kendall DP. Residual stresses and lifetimes of tubes subjected to shrink-fit prior to autofrettage. ASME J Pressure Vessel Technol 2003;125:282–6.
[16] Jahed H, Farshi B, Karimi M. Optimum autofrettage and shrink-fit combination in multi-layer cylinders. J Pressure Vessel Technol 2006;128:196–200.
[17] Parker AP. A Re-autofrettage procedure for mitigation of Bauschinger effect in thick cylinder. ASME J Pressure Vessel Technol 2004;126:451–545.
[18] Jahed H, Moghadam BA, Shambooli M. Re-autofrettage. J Pressure Vessel Technol 2006;128:223–6.
[19] Haghpanah Jahromi B, Farrahi GH, Maleki M, Nayeb-Hashemi H, Vaziri A. Residual stresses in autofrettaged vessel made of functionally graded material. Eng Struct 2009;31:2930–5.
[20] Nie GJ, Batra RC. Stress analysis and material tailoring in isotropic linear thermoelastic incompressible functionally graded rotating disks of variable thickness. Compos Struct 2010;92:720–9.
[21] Nie GJ, Batra RC. Material tailoring and analysis of functionally graded isotropic and incompressible linear elastic hollow cylinders. Compos Struct 2010;92:265–74.
[22] Shahzamanian MM, Sahari BB, Bayat M, Mustapha F, Ismarrubie ZN. Finite element analysis of thermoelastic contact problem in functionally graded axisymmetric brake disks. Compos Struct, in press. doi:1016/j.compstruct.2009.11.022.
[23] Tutuncu N, Temel B. A novel approach to stress analysis of pressurized FGM cylinders, disks and spheres. Compos Struct 2009;91:385–90.
[24] Timoshenko SP, Goodier JN. Theory of elasticity. McGraw-Hill; 1970.
[25] Schulz U, Peters M, Bach FW, Tegeder G. Graded coatings for thermal, wear and corrosion barriers. Mater Sci Eng A 2003;362:61–80.
[26] Suresh S. Graded materials for resistance to contact deformation and damage. Science 2001;292:2247–51.
[27] Cao XQ, Vassen R, Stoever D. Ceramic materials for thermal barrier coatings. J Eur Ceram Soc 2004;24:1–10.
[28] Evans AG, Mumm DR, Hutchinson JW, Meier GH, Pettit FS. Mechanisms controlling the durability of thermal barrier coatings. Prog Mater Sci 2001;46:505–53.
[29] Padture NP, Gell M, Jordan EH. Thermal barrier coatings for gas turbine engine applications. Science 2002;296:280–4.
[30] Freeman WT, Bryan CF, Macconochie IO, Breiner CA. Reusable cryogenic-liquid tank with replaceable liner. NASA Tech Brief LAR-14172 1984:431–2.
[31] Liu J, Hirano T. Design and analysis of FRP pressure vessels with load carrying metallic liners. ASME 1998;368:95–101.
[32] Barbero EJ, Wen EW. Autofrettage to offset coefficient of thermal expansion mismatch in metal-lined composite pipes. ASTMSTP 2003;1436:193–204.
[33] Suresh S, Mortensen A. Fundamentals of functionally graded materials. IOM Communications Ltd.; 1998.
[34] Gu Y, Nakamura T, Prchlik L, Sampath S, Wallace J. Micro-indentation and inverse analysis to characterize elastic–plastic graded materials. Mater Sci Eng A 2003;345:223–33.
[35] Kawasaki A, Watanabe R. Microstructural designing and fabrication of disk shaped functionally graded material by powder metallurgy. J Jpn Soc Powder Powder Metal 1990;37:253–8.
[36] Watannable R. Powder processing of functionally gradient materials. Mater Res Bull 1995;20:32–4.
[37] Sampath S, Hermann H, Shimoda N, Saito T. Thermal spray processing of FGMs. MRS Bull 1995;20:27–31.
[38] Miyamoto Y, Kaysser WA, Rabin BH. Functionally graded materials: design, processing and applications. Kluwer Academic Publishers; 1999.